

Reducing Overpotential of Lithium–Oxygen Batteries by Diatomic Metal Catalyst Orbital Matching Strategy

Aixiang Mao,[#] Jing Li,[#] Jia-hui Li,^{*} Honglai Liu, and Cheng Lian^{*}



Cite This: *J. Phys. Chem. Lett.* 2024, 15, 5501–5509



Read Online

ACCESS |



Metrics & More

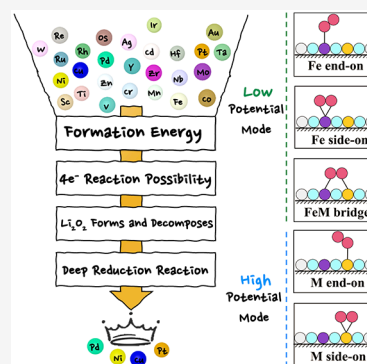


Article Recommendations

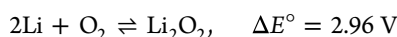


Supporting Information

ABSTRACT: Aprotic Li–O₂ batteries have sparked attention in recent years due to their ultrahigh theoretical energy density. Nevertheless, their practical implementation is impeded by the sluggish reaction kinetics at the cathode. Comprehending the catalytic mechanisms is pivotal to developing efficient cathode catalysts for high-performance Li–O₂ batteries. Herein, the intrinsic activity map of Li–O₂ batteries is established based on the specific adsorption mode of O₂ induced by diatomic catalyst orbital matching and the transfer–acceptance–backdonation mechanism, and the four-step screening strategy based on the intrinsic activity map is proposed. Guided by the strategy, FeNi@NC and FeCu@NC promising durable stability with a low overpotential are screened out from 27 Fe–Metal diatomic catalysts. Our research not only provides insights into the fundamental understanding of the reaction mechanism of Li–O₂ batteries but also accelerates the rational design of efficient Li–O₂ batteries based on the structure–activity relationship.



Aprotic lithium–oxygen (Li–O₂) batteries possess ultrahigh theoretical energy density of 3500 Wh kg⁻¹ and are deemed to be one of the most promising candidates as a power source for electric vehicles (EV).^{1–3} Typically, a rechargeable Li–O₂ battery consists of a lithium anode, a conductive electrolyte containing Li⁺, and a porous O₂ cathode. The core electrochemical reaction of Li–O₂ batteries is



It functions with the formation and decomposition of a series of lithium oxides through the oxygen reduction reaction (ORR, discharging process) and oxygen evolution reaction (OER, charging process).^{4,5} According to previous investigations,⁶ Li₂O₂ can be deeply reduced to Li₄O₂, which greatly increases the energy density of the cell through a reversible four-electron mechanism. Nonetheless, the sluggish reaction kinetics and formation of a parasitic product at the cathode can result in large overpotential,^{7–9} low discharge capacity,¹⁰ and poor cycle stability¹¹ under operating conditions, which severely hampers the commercial application of Li–O₂ batteries. As a result, numerous attempts have been dedicated to developing high-activity cathode catalysts for Li–O₂ batteries. Carbon materials, such as carbon nanotube¹² and graphene,¹³ possess exceptional electron conductivity and economical efficiency but must be replaced owing to electrolyte decomposition and formation of carbonate film at high charge voltage in order to enable the broader practical application.^{14–16} While noble-based catalysts, such as Pt, Au, and Ru,^{17–20} can address the stability concerns and maintain high ORR and OER activity, their commercialization is restricted by scarce reserves and high costs. Alternatively, two-dimensional (2D) transition

metal oxides (TMOs), such as Co₃O₄^{21,22} and RuO₂,²³ have drawn widespread interest because of their ample surface area for accommodation of lithium oxide intermediates and tunable electronic structure, but they usually own a wide band gap with low conductivity, which may further damage the cycle stability of the battery. Therefore, it is rather crucial but challenging for Li–O₂ batteries to rationally design cathode electrocatalysts simultaneously satisfying high activity, low cost, and durable stability.

Recently, atomically dispersed single-atom Fe–N–C catalysts^{24,25} that exhibit ORR activity (H₂–O₂ fuel cells) comparable to that of Pt/C, which is regarded as the benchmark of ORR catalysts, have attracted considerable interest owing to the maximized atomic utilization. On the basis of the single-atom catalysts (SACs),^{26,27} another active single atom is introduced to form a diatomic center which could combine the advantages of different atoms to achieve a win–win situation. Dual-atom catalysts (DACs) exhibit superior catalytic activity in various electrocatalytic reactions such as the hydrogen evolution reaction (HER),²⁸ ORR,²⁹ OER,³⁰ CO₂ reduction reaction (CO₂RR),³¹ nitrogen reduction reaction (NRR),³² and nitrate reduction reaction (NO₃RR).³³ Moreover, DACs with well-defined structure provide an ideal platform to examine the potential structure–

Received: April 21, 2024

Revised: May 9, 2024

Accepted: May 13, 2024

Published: May 15, 2024



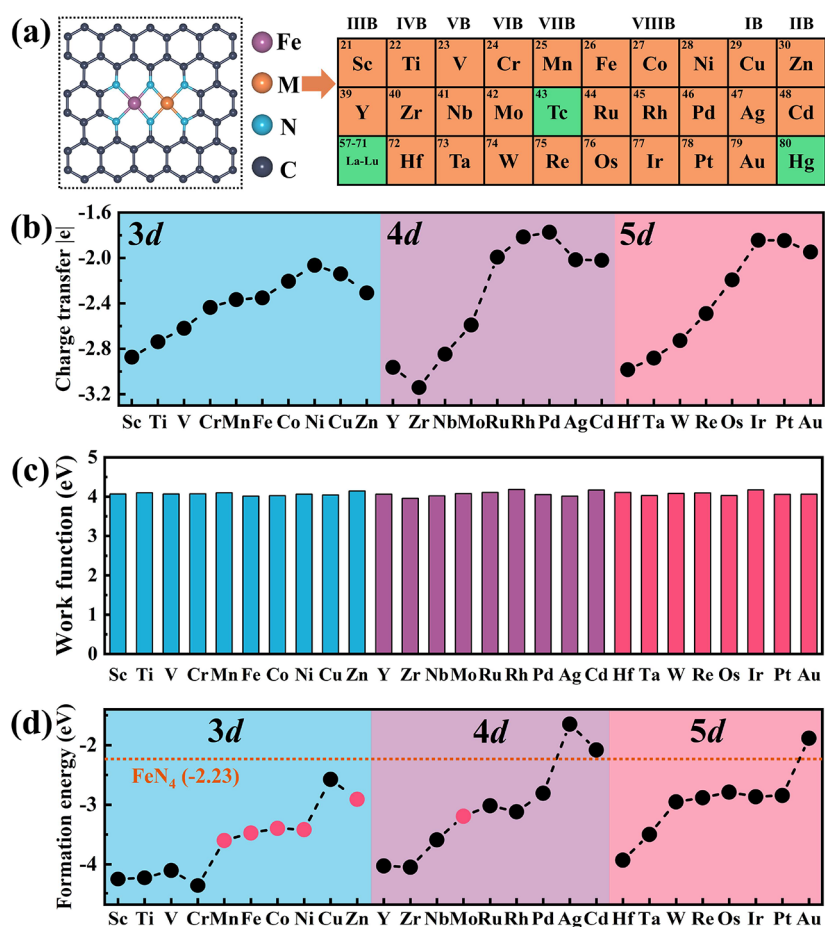


Figure 1. (a) Structural prototype of FeM@NC and 27 transition metals are taken into consideration in this work. (b) Comparison of transferred charge of FeM (M ranges from Sc to Au) dimers to the substrate. (c) The WF of the FeM@NC. (d) Computed formation energy of the FeM@NC.

activity relationship³⁴ at the atomic or molecular level by breaking the scaling relationship limitations. Nevertheless, the application of DACs in Li–O₂ batteries is scarcely reported, presenting a great obstacle to probing the catalytic mechanism of DACs in Li–O₂ batteries.

Herein, by means of large-scale density functional theory (DFT) calculations, we construct a series of FeM dimers embedded on a N-doped graphene monolayer (FeM@NC, M ranges from Sc to Au) to screen out promising cathode catalysts for Li–O₂ batteries with the help of a “four-step screening strategy”. We successfully obtain FeNi@NC and FeCu@NC exhibiting superior performance with a low total overpotential of 0.54 and 0.55 V, respectively. Moreover, they promise high thermodynamic stability confirmed by *ab initio* molecular dynamics (AIMD). More importantly, we establish the intrinsic activity map of Li–O₂ batteries based on the ability to capture electrons of O₂ from the substrate. Furthermore, the adsorption mode of O₂ plays a vital role in regulating the orbital matching between dual-atom and O₂, hence affecting the adsorption strength of O₂. This work paves new avenues for efficiently screening and rationally designing advanced electrocatalysts for Li–O₂ batteries and other multielectron reactions.

The FeN₄ SAC is established by replacing a C–C bond in the graphene monolayer with an Fe atom meanwhile coordinated with 4 N atoms (Figure S1). As shown in Figure 1a, the 3d, 4d, and 5d TM atoms are selected as dopant metal

M for FeN₄ with a total of 27 FeM dimers (except La groups, Tc, and Hg featuring toxicity or radioactivity). The optimized structures of these 27 catalysts are presented in Figure S2, where FeM dimers are in or out of the N-doped graphene plane primarily related to the radii of the TMs. Thirteen FeM dimers (M = Sc, Ti, Zn, Y, Zr, Nb, Mo, Ag, Cd, Hf, Ta, W, and Au) protrude from the N-doped graphene plane, resulting in the distorted configurations. In contrast, the remaining 14 FeM dimers are incorporated into the N-doped graphene, producing almost in-plane structures. The experimentally observed Fe–Mn bond length in FeMn@NC (2.5 Å)³⁵ is consistent with our calculated value of 2.5 Å (Table S1), which indicates the reliability of our calculation procedure. The distances between Fe and M atoms range from 2.30 (FeRu@NC) to 2.84 Å (FeY@NC) and show a parabolic trend across each period (Figure S3 and Table S1).

It is well-known that the simultaneous presence of dual active metal centers can induce unique electronic effects such as long-range interaction.³⁶ The significant charge (1.77–3.14 |e|) is transferred from the FeM dimers to the N-doped graphene monolayer, indicating the formation of strong TM–N bonds and then leading to high structural stability (Figure 1b). The charge transfer of FeM dimers exhibits an increasing trend across each period (Figure 1b), which is associated with electronegativity of doped TMs. More importantly, the positively charged FeM dimers due to their electron-losing properties (Figure 1b) can facilitate nucleophilic O₂ capture

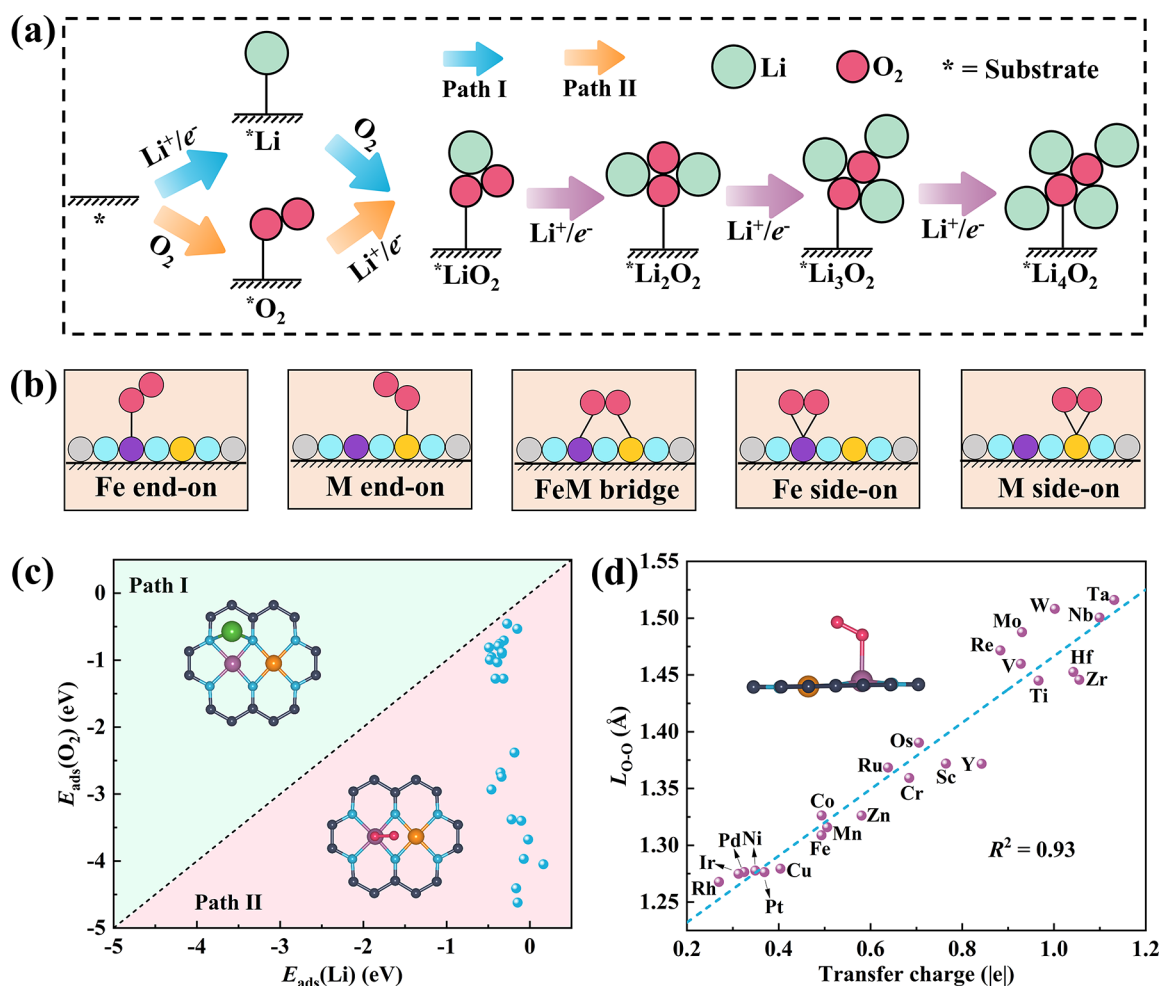


Figure 2. (a) Schematic diagram of reaction pathways for the ORR process of Li–O₂ batteries. (b) Five possible O₂ adsorption modes on the FeM@NC. (c) The $E_{\text{ads}}(\text{O}_2)$ and $E_{\text{ads}}(\text{Li})$ elucidates the nucleation pathway of LiO₂ on FeM@NC following Path II. (d) The correlation between the transferred charge during the O₂ adsorption process and O–O bond length of O₂.

and impede the Li⁺ adsorption, which determines the LiO₂ growth pathway. The calculated work function (WF) values (3.96–4.18 eV) for FeM@NC (Figure 1c) are considerably lower than that of semiconductor group III phosphide materials commonly utilized in electronic devices.³⁷ This suggests that electrons are prone to escape from FeM@NC along with enhanced electron conductivity facilitating the discharge and charge process of Li–O₂ batteries. Moreover, the Fe and M atoms exhibit a distinct loss of electrons (Table S1), which favors the adsorption and activation of linear molecules (such as O₂).³⁸

Generally, the electron transfer in the substrate can reflect the stability of the structure. For the FeN₄ configuration, the formation energy of Fe sites is –2.23 eV, indicating that the Fe atom on N-doped graphene is stable. Under the regulation of adjacent adsorption sites, the formation energy of FeM dimers ranges from –4.36 to –1.65 eV (Figure 1d). The introduction of an M atom on the FeN₄ nanosheet can manipulate the stability of FeM dimers. Among 27 doping systems, the relatively stable systems ($E_f < -2.23$ eV, lower formation energy than FeN₄) are chosen as candidates to explore the activity in Li–O₂ batteries. Hence, FeAg, FeCd, and FeAu are ruled out. Note that several systems marked in red have been synthesized practically, such as FeMn,³⁵ FeFe,³⁹ FeCo,⁴⁰

FeNi,⁴¹ FeZn,⁴² and FeMo,⁴³ thereby manifesting the feasibility of our first screening criteria.

The binding strength of O₂ and Li on the substrate plays a crucial role in determining the initial nucleation pathway of LiO₂. For the initial ORR process, two possible reaction pathways are taken into consideration (Figure 2a). Path I is understood as the favorable adsorption of Li, whereas path II signifies the initial adsorption of O₂. For the adsorption of Li on the substrate, we systematically investigate two adsorption sites of Li on the FeM@NC. Among 24 of 27 FeM@NC catalysts, the $E_{\text{ads}}(\text{Li})$ are concentrated in the energy level from –0.46 to 0.16 eV (Table S2). Compared with the $E_{\text{ads}}(\text{Li})$, $E_{\text{ads}}(\text{O}_2)$ shows different characteristics. Five possible O₂ adsorption modes are taken into account, including Fe end-on, M end-on, FeM bridge, Fe side-on, and M side-on mode (Figure 2b). After the full relaxation, there are only three stable adsorption modes for all 24 systems screened by the formation energy criteria, *i.e.*, Fe end-on, FeM bridge, and M side-on (Figure S4). As listed and shown in Table S2 and Figure S5, the $E_{\text{ads}}(\text{O}_2)$ for systems with Fe end-on mode is located between –0.46 and –0.81 eV, for FeM bridge mode is between –0.88 and –1.28 eV, and for M side-on mode is between –2.38 and –4.62 eV. Evidently, the $E_{\text{ads}}(\text{O}_2)$ strongly depends on the adsorption mode of O₂ (M side-on > FeM bridge > Fe end-on). Moreover, the $E_{\text{ads}}(\text{O}_2)$ values vary

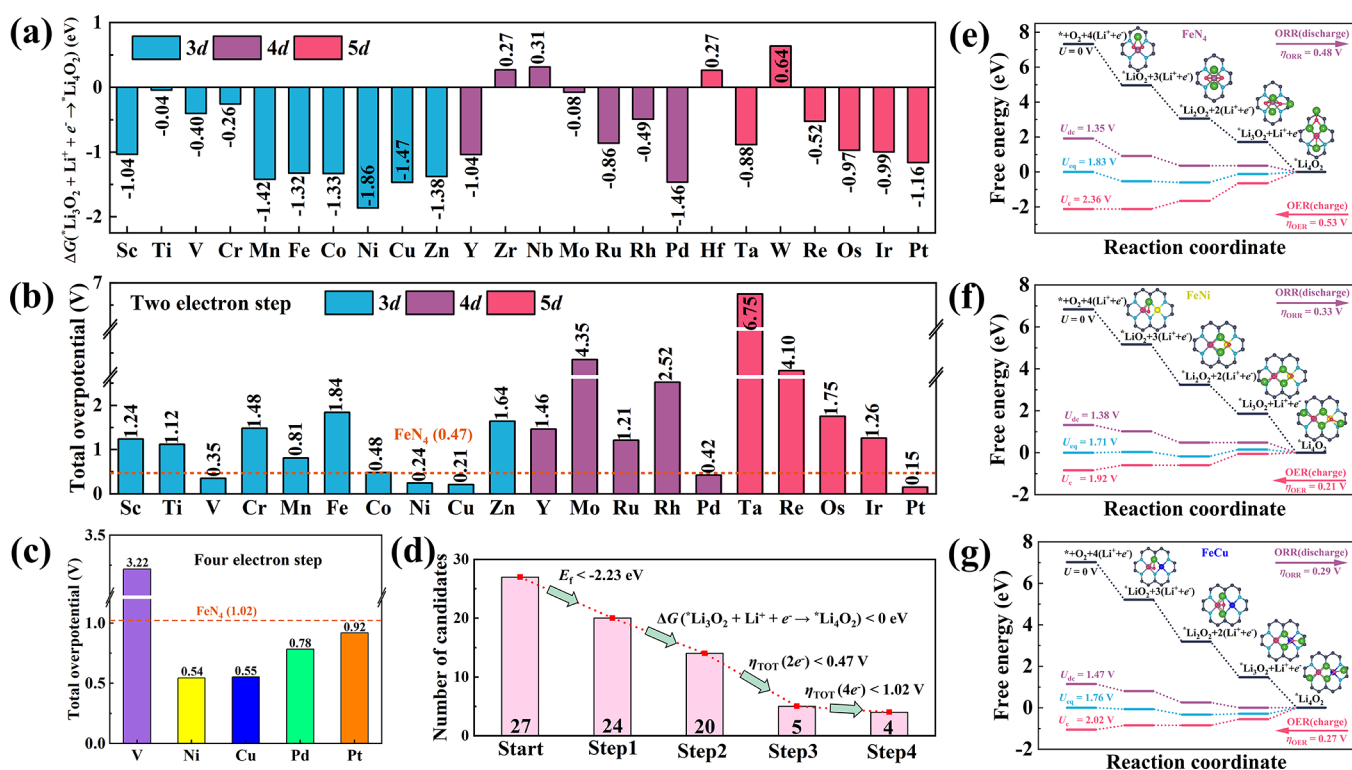
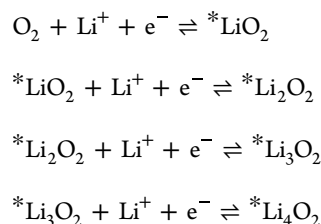


Figure 3. (a) The Gibbs free energy changes for $*\text{Li}_3\text{O}_2 + \text{Li}^+ + e^- \rightarrow *\text{Li}_4\text{O}_2$. (b) The total overpotential for two-electron step on 20 catalysts. (c) The total overpotential for four-electron steps for 5 promising FeM@NC candidates. (d) The “four-step screening strategy” is applied to identify the high-performance FeM@NC candidates. The Gibbs free energy diagram of the most favorable intermediate state for $*\text{LiO}_2$, $*\text{Li}_2\text{O}_2$, $*\text{Li}_3\text{O}_2$, and $*\text{Li}_4\text{O}_2$ at discharge, equilibrium, and charge potential for the four-electron mechanism on (e) FeN_4 , (f) FeNi @NC, and (g) FeCu @NC, respectively.

between -0.71 and -4.66 eV (Table S2), which are all larger than $E_{\text{ads}}(\text{Li})$, indicating O_2 is more advantageous to adsorb than Li on the FeM@NC monolayer (Figure 2c). As a result, the positively charged FeM dimers are desired to adsorb the nucleophilic O_2 molecule and then react with Li^+ to form LiO_2 ; that is, the formation pathway of LiO_2 follows path II, and the adsorption and activation of O_2 becomes a prerequisite of the discharging process in Li– O_2 batteries.

After O_2 adsorption on the FeM@NC, the O–O bond length (1.27–1.52 Å) is elongated compared with a free O_2 molecule (1.23 Å), implying sufficient activation of O_2 on the FeM@NC. Moreover, a good linear relationship ($R^2 = 0.93$) between electrons received by O_2 and O–O bond length is established (Figure 2d). Therefore, the charge transferred can serve as an efficient descriptor to elucidate the activation degree of the O_2 molecule. To be specific, the more the electrons O_2 gains, the higher the activation degree of O_2 .

Given the complexity of the electrochemical reaction in Li– O_2 batteries, efficient filtering descriptors are indispensable. Therefore, a “four-step screening strategy” is proposed to assess proper cathode catalysts to achieve high-performance Li– O_2 batteries (Figure 3d). As mentioned above, the structure stability of the substrate is a vital evaluation criterion for the practical application of Li– O_2 batteries. Compared with the formation energy of FeN_4 (-2.23 eV), more energy is released during the formation of 24 of 27 FeM dimers, which is the first criterion in the “four-step screening strategy”. The second criterion starts from the specific reaction mechanism of the batteries. The discharging/charging process of Li– O_2 batteries could be described by the four reaction steps:



where * represents the cathode catalysts and $*\text{Li}_x\text{O}_2$ intermediates adsorbed on the substrate denote discharge product of each reaction step during the ORR process. In aprotic Li– O_2 batteries, Li_2O_2 could be intermediates and further reduced to Li_4O_2 under certain catalysts, accompanied by a four-electron transfer. Therefore, two possible reaction mechanisms (the two-electron mechanism, $\text{O}_2 + 2\text{Li}^+ + 2e^- \rightleftharpoons \text{Li}_2\text{O}_2$, and the four-electron mechanism, $\text{O}_2 + 4\text{Li}^+ + 4e^- \rightleftharpoons \text{Li}_4\text{O}_2$) are taken into consideration depending on the final discharge product (Li_2O_2 or Li_4O_2). Furthermore, the four-electron mechanism can provide greater discharge capacity. Figure 3a depicts the Gibbs free energy changes of the $*\text{Li}_4\text{O}_2$ formation step ($*\text{Li}_3\text{O}_2 + \text{Li}^+ + e^- \rightarrow *\text{Li}_4\text{O}_2$), which is typically considered as rate-determining step (RDS) of the four-electron ORR process in Li– O_2 batteries⁴⁴ because of similar adsorption strength of Li_3O_2 and Li_4O_2 (Table S2). To guarantee the spontaneous proceeding of the four-electrons discharging process and improve discharge capacity for Li– O_2 batteries, the free energy change of four-electron deep reduction reaction should be less than 0 eV. In this step, 20 of 24 FeM@NC systems meet screening criteria, namely, Zr, Nb, Hf, and W doped systems are screened out (Figure 3a). On the basis of the reaction free energy of each step (Figures

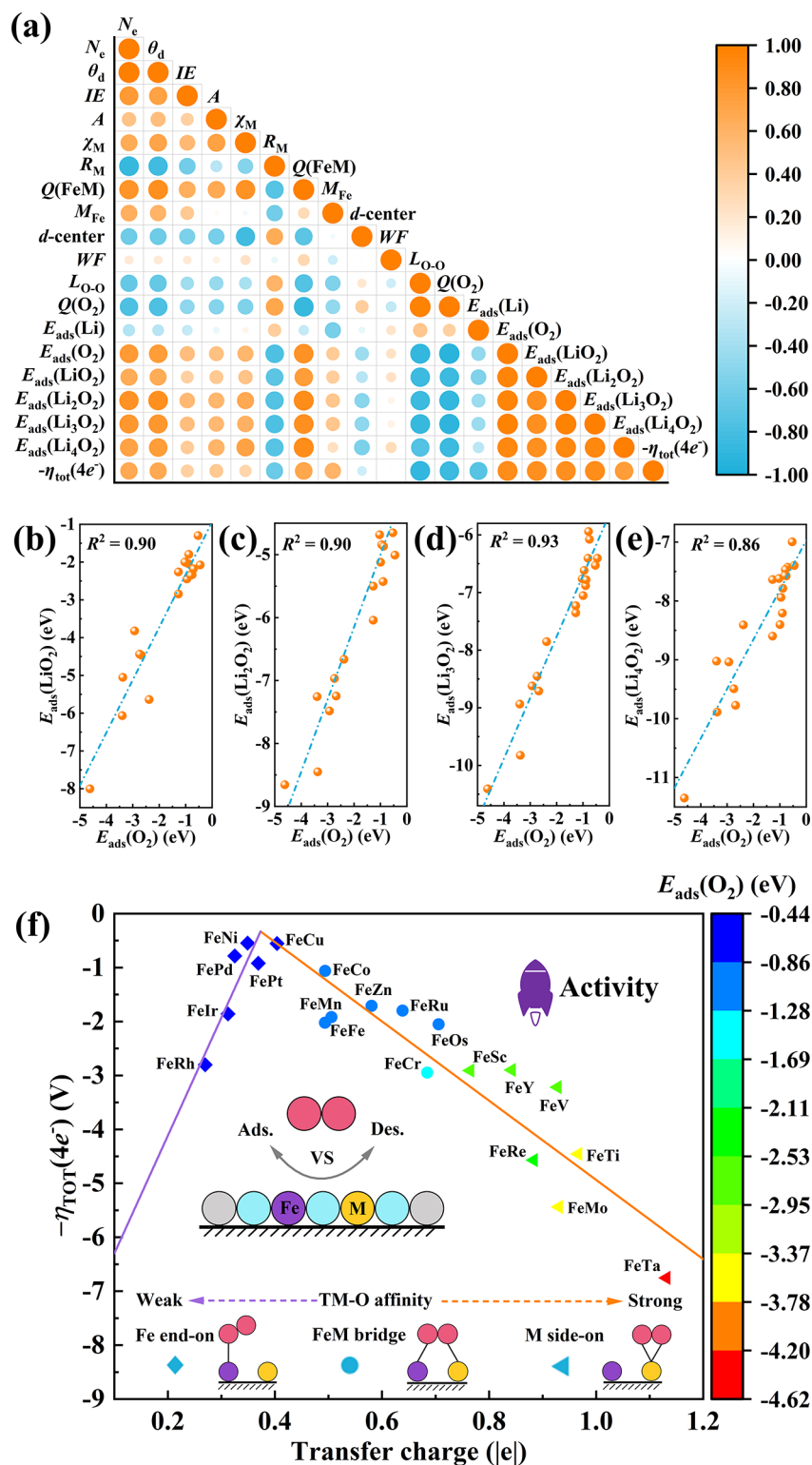


Figure 4. (a) Heat map created to illustrate the Pearson correlation matrix between each of the 18 primary features. N_e is the valence electron number of M; θ_d is the electron number of d orbital of M; IE is the first ionization energy of M; A is the electron affinity energy of M; χ_M is the Pauling electronegativity of M; R_M is the atomic radius of M; $Q(\text{FeM})$ is the charge transfer from FeM dimers to the supports; $d\text{-center}$ is the d -band center of Fe; $Q(\text{O}_2)$ is the charge transfer from the substrate to O_2 . The correlation between the (b) $E_{\text{ads}}(\text{LiO}_2)$, (c) $E_{\text{ads}}(\text{Li}_2\text{O}_2)$, (d) $E_{\text{ads}}(\text{Li}_3\text{O}_2)$, and (e) $E_{\text{ads}}(\text{Li}_4\text{O}_2)$ and the $E_{\text{ads}}(\text{O}_2)$ on 20 FeM@NC catalysts. (f) Volcano plot for $-\eta_{\text{TOT}}(4e^-)$ versus the descriptor $Q(\text{O}_2)$ (transfer charge).

S6–S8), the U_{d^*} , U_{O^*} , and U_{e^*} are determined and then η_{ORR} , η_{OER} , and η_{TOT} are used to evaluate the catalytic activity of FeM@NC. The $\eta_{\text{TOT}}(2e^-)$ of FeN_4 is 0.47 V, which is

regarded as the third screening criterion in the “four-step screening strategy” (Figure 3b). Five FeM dimers, namely, FeV, FeNi, FeCu, FePd, and FePt, are screened after three

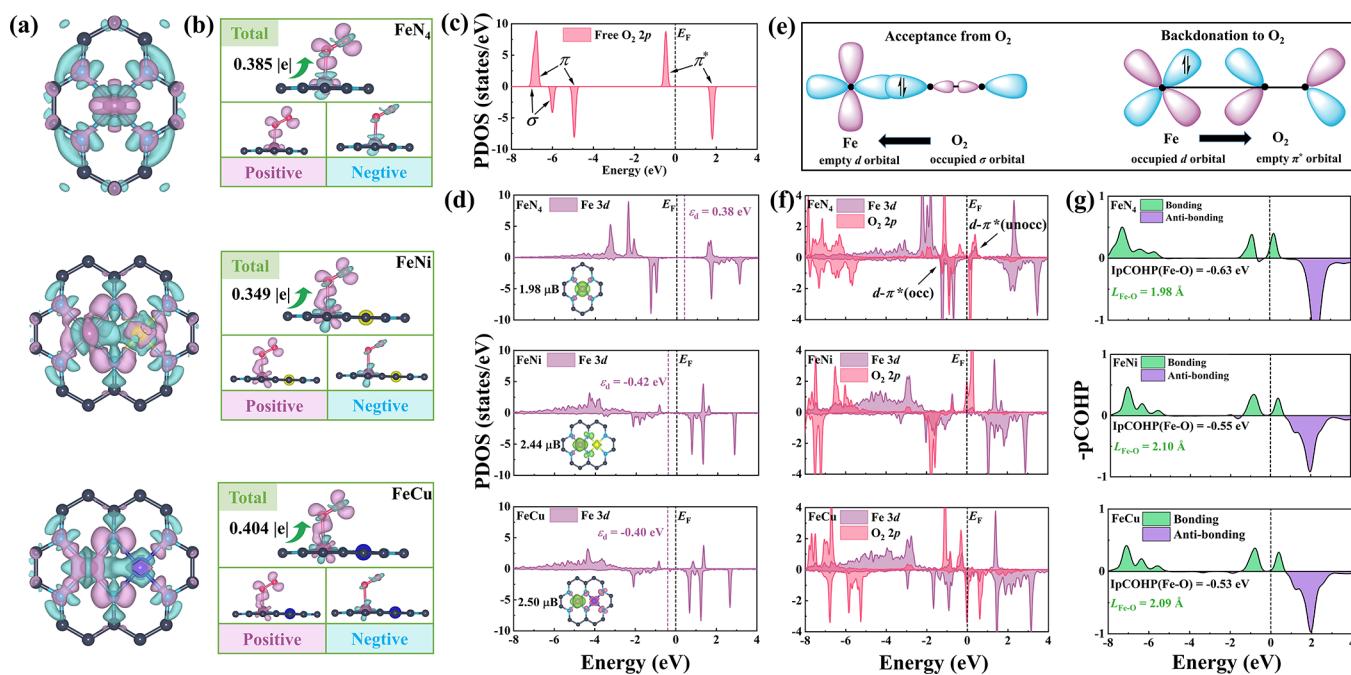


Figure 5. CDD of FeN₄, FeNi@NC, and FeCu@NC (a) before and (b) after O₂ adsorption, where the purple and blue colors represent the charge accumulation and depletion zones, respectively. The isosurface value is 0.005 e bohr⁻³. (c) The PDOS of free O₂ molecule. (d) The PDOS of FeN₄, FeNi@NC, and FeCu@NC with corresponding spin density and magnetic moment. (e) The simplified scheme of acceptance–backdonation between Fe and O₂. (f) The PDOS and (g) the pCOHP of O₂ adsorbed FeN₄, FeNi@NC, and FeCu@NC.

screening steps (Figure 3b). Finally, with the help of the $\eta_{\text{TOT}}(4e^-)$ (1.02 V) of FeN₄, four catalysts (FeNi, FeCu, FePd, and FePt) are screened out for the promising catalysts with the $\eta_{\text{TOT}}(4e^-)$ of 0.54, 0.55, 0.78, and 0.92 V, respectively. Especially FeNi and FeCu stand out with the lowest $\eta_{\text{TOT}}(4e^-)$ (Figure 3c), and their stabilities are proven to be high at various temperature (Figures S15–S18).

Figure 3e–g depicts the free energy profiles along the four-electron mechanism (*O₂, *LiO₂, *Li₂O₂, *Li₃O₂, and *Li₄O₂) catalyzed by FeN₄, FeNi, and FeCu under diverse potentials with optimized Li_xO₂ intermediate adsorption configuration. For these three systems, all reaction steps are exothermic and proceed spontaneously at open-circuit voltage ($U = 0$ V). During the discharge process, the discharge potential of FeN₄, FeNi, and FeCu is 1.35, 1.38, and 1.47 V, respectively. When the applied charge potential reaches 2.36, 1.92, and 2.02 V for FeN₄, FeNi, and FeCu, the whole charging process keeps the downhill trend of Gibbs free energy.

To quantitatively measure the catalytic performance of these systems, discharge overpotential η_{ORR} and charge overpotential η_{OER} for FeN₄, FeNi, and FeCu are displayed in Figure 3e–g. The $\eta_{\text{ORR}}/\eta_{\text{OER}}$ values of FeNi (0.33/0.21 V) and FeCu (0.29/0.27 V) are much lower than that of FeN₄ (0.48/0.53 V), exhibiting excellent catalytic performance in Li–O₂ batteries, which could be attributed to the adsorption strength balance of lithium–oxygen intermediates. In other words, the interaction difference of the Li_xO₂ intermediates can be averaged under the catalysis of FeNi and FeCu (Figure S9), which is in accordance with previous research.⁴⁵

A complete activity map needs to be established to elucidate the activity origin of the promising catalysts FeNi@NC and FeCu@NC. To evaluate the total overpotential of the four-electron mechanism, the free energy diagrams are constructed based on the energetics of all reaction intermediates. This is a multifactor issue that requires minimizing the number of

parameters to simplify the problem and enable the rational design of catalysts. The Pearson correlation map demonstrates that $E_{\text{ads}}(\text{O}_2)$ and $E_{\text{ads}}(\text{LiO}_2)$, $E_{\text{ads}}(\text{Li}_2\text{O}_2)$, $E_{\text{ads}}(\text{Li}_3\text{O}_2)$, $E_{\text{ads}}(\text{Li}_4\text{O}_2)$ have a strong positive correlation with corresponding Pearson correlation coefficients of 0.95, 0.95, 0.96, and 0.93, respectively (Figure 4a). Moreover, the $E_{\text{ads}}(\text{LiO}_2)$, $E_{\text{ads}}(\text{Li}_2\text{O}_2)$, $E_{\text{ads}}(\text{Li}_3\text{O}_2)$, and $E_{\text{ads}}(\text{Li}_4\text{O}_2)$ is strongly positively correlated with the $E_{\text{ads}}(\text{O}_2)$ in the wide range from -5 to 0 eV (Figure 4b–e). As displayed in Figures S10–S14, $E_{\text{ads}}(\text{Li}_x\text{O}_2)$ and $-\eta_{\text{TOT}}(4e^-)$ promise a weak correlation. Meanwhile, the Pearson correlation coefficient between $E_{\text{ads}}(\text{O}_2)$, $E_{\text{ads}}(\text{LiO}_2)$, $E_{\text{ads}}(\text{Li}_2\text{O}_2)$, $E_{\text{ads}}(\text{Li}_3\text{O}_2)$, $E_{\text{ads}}(\text{Li}_4\text{O}_2)$, and $-\eta_{\text{TOT}}(4e^-)$ is 0.88, 0.87, 0.87, 0.89, and 0.76, respectively (Figure 4a). Considering the association of O₂ adsorption and activation mode and battery performances, we construct a volcano relationship between the $E_{\text{ads}}(\text{O}_2)$ determined by Bader charge transfer during the adsorption process and $-\eta_{\text{TOT}}(4e^-)$ (Figure 4f), which breaks the linear relationship. Specifically, we discover that an appropriate interaction strength between O₂ and FeM dimers with a charge transfer from 0.32 to 0.40 |e| can balance the energy changes of activation of O₂ in the discharging process and the desorption of O₂ in the charging process, achieving the optimal ORR and OER performance with a low overpotential. More importantly, the volcano relationship can be divided into three zones according to the O₂ adsorption modes (Fe end-on, FeM bridge, and M side-on), indicating the catalyst activity origin is highly correlated with the adsorption mode of O₂. Moreover, all catalysts with high activity (i.e., the most promising catalysts screened by our “four-step screening strategy”) promise O₂ with Fe end-on adsorption mode. Therefore, the adsorption modes of O₂ play a crucial role in determining the performance of Li–O₂ batteries. Moreover, as the result of the “four-step screening strategy” (Figure 3), the Fe–M bond length of these four promising electrocatalysts (FeNi, FeCu, FePd, and FePt)

gather between 2.45 and 2.47 Å, distinguished from other electrocatalysts (Figure S3 and Table S1), which demonstrates that an appropriate bond length is crucial for the performance of Li–O₂ batteries catalyzed by dual atoms.

The charge density difference (CDD) and the partial density of states (PDOS) of O₂ adsorbed on the FeN₄, FeNi, and FeCu is calculated to explore the activation origin of O₂ with Fe end-on adsorption mode. The significant charge transfer (0.349–0.404 |e|) between Fe and O₂ can be observed (Figure S5b). The charge transfer here is a two-way process, where the charge accumulation and depletion can be observed for both Fe and O₂. As a result, O₂ can be activated through the acceptance–backdonation mechanism, where Fe can receive the lone-pair electrons from the O₂ and simultaneously backdonate electrons to antibonding orbitals of O₂ (Figure S5e). As shown in Figure 5a, without the adsorption of O₂, the Fe and Ni/Cu atoms of FeNi@NC and FeCu@NC serve as the electron accumulation and depletion centers, respectively, demonstrating that the Fe atom can accept electrons from Ni and Cu and thus realizing a subtle regulation on the electronic structure of Fe active center.

To unravel deeply the underlying mechanism of O₂ activation, the PDOS without and with O₂ adsorbed on FeN₄, FeNi@NC, and FeCu@NC is employed to investigate the electronic interactions between the Fe and O₂ (Figure S5d–f). After the introduction of Ni and Cu single atom on FeN₄, the *d*-electron of Fe undergoes delocalization along with the decrease of the *d* band center of Fe, implying the weakening of O₂ adsorption strength on the substrate (Figure S5d). Moreover, the magnetic moment of Fe increases from 1.98 to 2.44 and 2.50 μ_B for FeN₄, FeNi, and FeCu along with the spin transition from the low spin state (LS) to high spin state (HS), but there is no high spin transformation of Fe in FeRh and FeIr (Table S1). Therefore, HS is beneficial to the activation of triplet oxygen, which is consistent with relevant reports.⁴⁶ For the free O₂ molecule, three characteristic molecular orbitals (σ , π , and π^*) can be observed within the energy range spanning from –8 to 4 eV (Figure 5c). After O₂ adsorbed on FeN₄, FeNi, and FeCu, the phenomenon of acceptance–backdonation can also be observed at two energy windows (Figure 5f). When O₂ is adsorbed on the FeN₄, the σ orbital of O₂ transfers electrons to the empty *d* orbital of Fe in the energy level from –8 to –5 eV, forming the bonding states to enhance the O₂ adsorption. Meanwhile, the occupied *d* orbital of Fe backdonates electrons to the π^* orbital of O₂ in the energy level from –3 to 0 eV, leading to the partially filled π^* orbital near the Fermi level (E_F). On the other hand, the *d* electrons of Fe are more delocalized during the *d*– π^* interactions of the backdonation process attributed to the regulation of another adsorption site (Ni and Cu), leading to weaker O₂ adsorption strength. As a result, compared with the molecular orbitals of free O₂ gas, the ability of the Fe center to adsorb and activate O₂ can be attributed to its empty and occupied *d* orbitals.

For a deep insight into the *d*– π^* interactions quantitatively during the backdonation process, the projected crystal orbital Hamilton population (pCOHP) of Fe–O bond analysis is performed. In addition, we also calculate the integrated pCOHP (IpCOHP) by calculating the energy integral up to the highest occupied (below E_F), which directly gives more quantitative information. The more negative the IpCOHP value, the lower the bonding orbital energy level, the more stable the bond. The computed IpCOHP for FeN₄ (–0.63 eV)

is more negative than FeNi (–0.55 eV) and FeCu (–0.53 eV) with the stretching of the Fe–O bond (2.10 and 2.09 Å) (Figure 5g), which is consistent with the above analysis and conclusions. Through the CDD and PDOS analysis, the acceptance–backdonation mechanism has been validated. As a consequence, the activity origin of the promising catalysts FeNi and FeCu with O₂ Fe end-on mode can be attributed to the acceptance–backdonation mechanism between Fe and O₂.

In summary, extensive DFT calculations are performed to systematically investigate the potential of FeM dimers embedded in N-doped graphene for Li–O₂ batteries. We reveal that the activity of Li–O₂ battery cathode catalysts originates from the activation of O₂ with the specific adsorption mode, which can be modulated by the design of diatomic catalysts. With the helping hand of a “four-step screening strategy” (the formation energy E_f , the Gibbs free energy change of RDS, the two-electron step total overpotential $\eta_{TOT}(2e^-)$, and the four-electron step total overpotential $\eta_{TOT}(4e^-)$), FeNi@NC, FeCu@NC, FePd@NC, and FePt@NC are screened out from 27 FeM@NC candidates with the low $\eta_{TOT}(4e^-)$; especially, FeNi@NC and FeCu@NC stand out with the lowest $\eta_{TOT}(4e^-)$ of 0.54 and 0.55 V and high structure stability to the organic molecules (DMSO and DME). To unveil the activity origin of FeM@NC in Li–O₂ batteries, the activation of O₂ is closely correlated to the total overpotential $\eta_{TOT}(4e^-)$. Moreover, FeCu and FeNi with Fe end-on adsorption mode promise the best performance in Li–O₂ batteries, which can be attributed to the regulation of additional active center on the dual metal atom orbital matching mechanism with electron transfer–acceptance–backdonation between the Fe active center and O₂. The dual-atom acceptance–backdonation mechanisms may offer new insights toward the modification of catalysts for the process involving the activation of oxygen molecules and promote the rational design of high-efficiency catalysts.

■ ASSOCIATED CONTENT

Supporting Information

The Supporting Information is available free of charge at <https://pubs.acs.org/doi/10.1021/acs.jpcllett.4c01160>.

Computation methods and detailed discussion about the stability of FeNi@NC and FeCu@NC; optimized structure of 27 FeM@NC monolayers and O₂ adsorbed on the 24 FeM@NC; Gibbs free energy diagram of the most favorable intermediate state for *LiO₂, *Li₂O₂, *Li₃O₂, and *Li₄O₂ at the discharge, equilibrium, and charge potential for the four-electron mechanism on the 20 FeM@NC; correlation between the $E_{ads}(O_2)$, $E_{ads}(LiO_2)$, $E_{ads}(Li_2O_2)$, $E_{ads}(Li_3O_2)$, and $E_{ads}(Li_4O_2)$ on these 20 FeM@NC monolayers and the $-\eta_{TOT}(4e^-)$; and the side views of the snapshot of FeNi@NC and FeCu@NC after AIMD simulation under various temperatures for 10 ps with a time step of 2 fs (PDF)

■ AUTHOR INFORMATION

Corresponding Authors

Jia-hui Li – School of Chemistry and Molecular Engineering, East China University of Science and Technology, Shanghai 200237, P. R. China; orcid.org/0000-0002-0985-0525; Email: jiahui@ecust.edu.cn

Cheng Lian – School of Chemistry and Molecular Engineering and State Key Laboratory of Chemical Engineering, Shanghai

Engineering Research Center of Hierarchical Nanomaterials, School of Chemical Engineering, East China University of Science and Technology, Shanghai 200237, P. R. China;

orcid.org/0000-0002-9016-832X; Email: liancheng@ecust.edu.cn

Authors

Aixiang Mao – School of Chemistry and Molecular Engineering, East China University of Science and Technology, Shanghai 200237, P. R. China

Jing Li – School of Chemistry and Molecular Engineering, East China University of Science and Technology, Shanghai 200237, P. R. China

Honglai Liu – School of Chemistry and Molecular Engineering and State Key Laboratory of Chemical Engineering, Shanghai Engineering Research Center of Hierarchical Nanomaterials, School of Chemical Engineering, East China University of Science and Technology, Shanghai 200237, P. R. China; orcid.org/0000-0002-5682-2295

Complete contact information is available at:

<https://pubs.acs.org/10.1021/acs.jpcllett.4c01160>

Author Contributions

#A.M. and J.L. contributed equally to this work.

Notes

The authors declare no competing financial interest.

ACKNOWLEDGMENTS

This work was supported by the Fundamental Research Funds for the Central Universities (No. 2022ZJFH004), the National Natural Science Foundation of China (No. 22308096, No. 22278127, and No. 22378112), and the Shanghai Pilot Program for Basic Research (No. 22T01400100-18).

REFERENCES

- (1) Aurbach, D.; McCloskey, B. D.; Nazar, L. F.; Bruce, P. G. Advances in understanding mechanisms underpinning lithium-air batteries. *Nat. Energy* **2016**, *1* (9), No. 16128.
- (2) Zhang, P.; Zhao, Y.; Zhang, X. Functional and stability orientation synthesis of materials and structures in aprotic Li–O₂ batteries. *Chem. Soc. Rev.* **2018**, *47* (8), 2921–3004.
- (3) Kwak, W.-J.; Rosy; Sharon, D.; Xia, C.; Kim, H.; Johnson, L. R.; Bruce, P. G.; Nazar, L. F.; Sun, Y.-K.; Frimer, A. A.; Noked, M.; Freunberger, S. A.; Aurbach, D. Lithium–Oxygen Batteries and Related Systems: Potential, Status, and Future. *Chem. Rev.* **2020**, *120* (14), 6626–6683.
- (4) Lv, Q.; Zhu, Z.; Ni, Y.; Geng, J.; Li, F. Spin-State Manipulation of Two-Dimensional Metal–Organic Framework with Enhanced Metal–Oxygen Covalency for Lithium–Oxygen Batteries. *Angew. Chem., Int. Ed.* **2022**, *61* (8), No. e202114293.
- (5) Ouyang, H.; Min, S.; Yi, J.; Liu, X.; Ning, F.; Qin, J.; Jiang, Y.; Zhao, B.; Zhang, J. Tuning composite solid-state electrolyte interface to improve the electrochemical performance of lithium–oxygen battery. *Green Energy Environ* **2023**, *8* (4), 1195–1204.
- (6) Xia, C.; Kwok, C. Y.; Nazar, L. F. A high-energy-density lithium–oxygen battery based on a reversible four-electron conversion to lithium oxide. *Science* **2018**, *361* (6404), 777–781.
- (7) Zhou, Y.; Yin, K.; Gu, Q.; Tao, L.; Li, Y.; Tan, H.; Zhou, J.; Zhang, W.; Li, H.; Guo, S. Lewis-Acidic PtIr Multipods Enable High-Performance Li–O₂ Batteries. *Angew. Chem., Int. Ed.* **2021**, *60* (S1), 26592–26598.
- (8) Wang, W.; Tan, C.; He, L.; Yu, F.; Gao, X.; Chen, Y. Determinants of the Surface Film during the Discharging Process in Lithium–Oxygen Batteries. *J. Phys. Chem. Lett.* **2024**, *15* (2), 583–589.
- (9) Xiong, L.; Su, N. Q.; Fang, W.-H. The Role of Self-Catalysis Induced by Co Doping in Nonaqueous Li–O₂ Batteries. *J. Phys. Chem. Lett.* **2023**, *14* (33), 7526–7540.
- (10) Zhang, J.; Zhao, Y.; Sun, B.; Xie, Y.; Tkacheva, A.; Qiu, F.; He, P.; Zhou, H.; Yan, K.; Guo, X.; Wang, S.; McDonagh, A. M.; Peng, Z.; Lu, J.; Wang, G. A long-life lithium–oxygen battery via a molecular quenching/mediating mechanism. *Sci. Adv.* **2022**, *8* (3), eabm1899.
- (11) Zhou, Y.; Gu, Q.; Yin, K.; Li, Y.; Tao, L.; Tan, H.; Yang, Y.; Guo, S. Engineering eg Orbital Occupancy of Pt with Au Alloying Enables Reversible Li–O₂ Batteries. *Angew. Chem., Int. Ed.* **2022**, *61* (26), No. e202201416.
- (12) Lim, H.-D.; Park, K.-Y.; Song, H.; Jang, E. Y.; Gwon, H.; Kim, J.; Kim, Y. H.; Lima, M. D.; Robles, R. O.; Lepřo, X.; Baughman, R. H.; Kang, K. Enhanced Power and Rechargeability of a Li–O₂ Battery Based on a Hierarchical-Fibril CNT Electrode. *Adv. Mater.* **2013**, *25* (9), 1348–1352.
- (13) Xiao, J.; Mei, D.; Li, X.; Xu, W.; Wang, D.; Graff, G. L.; Bennett, W. D.; Nie, Z.; Saraf, L. V.; Aksay, I. A.; Liu, J.; Zhang, J.-G. Hierarchically Porous Graphene as a Lithium–Air Battery Electrode. *Nano Lett.* **2011**, *11* (11), 5071–5078.
- (14) Ottakam Thotiyl, M. M.; Freunberger, S. A.; Peng, Z.; Bruce, P. G. The Carbon Electrode in Nonaqueous Li–O₂ Cells. *J. Am. Chem. Soc.* **2013**, *135* (1), 494–500.
- (15) Freunberger, S. A.; Chen, Y.; Peng, Z.; Griffin, J. M.; Hardwick, L. J.; Bardé, F.; Novák, P.; Bruce, P. G. Reactions in the Rechargeable Lithium–O₂ Battery with Alkyl Carbonate Electrolytes. *J. Am. Chem. Soc.* **2011**, *133* (20), 8040–8047.
- (16) Mahne, N.; Renfrew, S. E.; McCloskey, B. D.; Freunberger, S. A. Electrochemical Oxidation of Lithium Carbonate Generates Singlet Oxygen. *Angew Chem Int Ed* **2018**, *57* (19), 5529–5533.
- (17) Kwak, K.-H.; Kim, D. W.; Kang, Y.; Suk, J. Hierarchical Ru- and RuO₂-foams as high performance electrocatalysts for rechargeable lithium–oxygen batteries. *J. Mater. Chem. A* **2016**, *4* (42), 16356–16367.
- (18) Luo, Z.; Li, F.; Hu, C.; Li, D.; Cao, Y.; Scott, K.; Gong, X.; Luo, K. Impact of a Gold Nanocolloid Electrolyte on Li₂O₂ Morphology and Performance of a Lithium–Oxygen Battery. *ACS Appl. Mater. Interfaces* **2021**, *13* (3), 4062–4071.
- (19) Zhang, E.; Dong, A.; Yin, K.; Ye, C.; Zhou, Y.; Tan, C.; Li, M.; Zheng, X.; Wang, Y.; Gao, X.; Li, H.; Wang, D.; Guo, S. Electron Localization in Rationally Designed Pt1Pd Single-Atom Alloy Catalyst Enables High-Performance Li–O₂ Batteries. *J. Am. Chem. Soc.* **2024**, *146* (4), 2339–2344.
- (20) Liu, L.; Zhou, C.; Fang, W.; Hou, Y.; Wu, Y. Rational design of Ru/TiO₂/CNTs as cathode: promotion of cycling performance for aprotic lithium–oxygen battery. *Energy Mater.* **2023**, *3* (2), No. 300011.
- (21) Song, K.; Cho, E.; Kang, Y.-M. Morphology and Active-Site Engineering for Stable Round-Trip Efficiency Li–O₂ Batteries: A Search for the Most Active Catalytic Site in Co₃O₄. *ACS Catal.* **2015**, *5* (9), 5116–5122.
- (22) Lin, Y.; Yang, Q.; Geng, F.; Feng, H.; Chen, M.; Hu, B. Suppressing Singlet Oxygen Formation during the Charge Process of Li–O₂ Batteries with a Co₃O₄ Solid Catalyst Revealed by Operando Electron Paramagnetic Resonance. *J. Phys. Chem. Lett.* **2021**, *12* (42), 10346–10352.
- (23) Shi, L.; Xu, A.; Zhao, T. RuO₂ Monolayer: A Promising Bifunctional Catalytic Material for Nonaqueous Lithium–Oxygen Batteries. *J. Phys. Chem. C* **2016**, *120* (12), 6356–6362.
- (24) Jiang, R.; Li, L.; Sheng, T.; Hu, G.; Chen, Y.; Wang, L. Edge-Site Engineering of Atomically Dispersed Fe–N₄ by Selective C–N Bond Cleavage for Enhanced Oxygen Reduction Reaction Activities. *J. Am. Chem. Soc.* **2018**, *140* (37), 11594–11598.
- (25) Scharf, J.; Kübler, M.; Gridin, V.; Wallace, W. D. Z.; Ni, L.; Paul, S. D.; Kramm, U. I. Relation between half-cell and fuel cell activity and stability of FeNC catalysts for the oxygen reduction reaction. *SusMat* **2022**, *2* (5), 630–645.
- (26) Li, Y.; Ren, P.; Lu, X.; Zhang, J.; Yang, P.; Yang, X.; Wang, G.; Liu, A.; Wu, G.; An, M. Elucidating the role of P on Mn- and N-

doped graphene catalysts in promoting oxygen reduction: Density functional theory studies. *SusMat* **2023**, *3* (3), 390–401.

(27) Xia, Q.; Zhai, Y.; Zhao, L.; Wang, J.; Li, D.; Zhang, L.; Zhang, J. Carbon-supported single-atom catalysts for advanced rechargeable metal-air batteries. *Energy Mater.* **2022**, *2* (3), No. 200015.

(28) Zhang, X.; Chen, A.; Zhang, Z.; Jiao, M.; Zhou, Z. Transition metal anchored C₂N monolayers as efficient bifunctional electrocatalysts for hydrogen and oxygen evolution reactions. *J. Mater. Chem. A* **2018**, *6* (24), 11446–11452.

(29) Liu, J.; Xu, H.; Zhu, J.; Cheng, D. Understanding the Pathway Switch of the Oxygen Reduction Reaction from Single- to Double-/Triple-Atom Catalysts: A Dual Channel for Electron Acceptance–Backdonation. *JACS Au* **2023**, *3* (11), 3031–3044.

(30) Pei, Z.; Lu, X. F.; Zhang, H.; Li, Y.; Luan, D.; Lou, X. W. Highly Efficient Electrocatalytic Oxygen Evolution Over Atomically Dispersed Synergistic Ni/Co Dual Sites. *Angew. Chem., Int. Ed.* **2022**, *61* (40), No. e202207537.

(31) Karmodak, N.; Vijay, S.; Kastlunger, G.; Chan, K. Computational Screening of Single and Di-Atom Catalysts for Electrochemical CO₂ Reduction. *ACS Catal.* **2022**, *12* (9), 4818–4824.

(32) Lv, X.; Wei, W.; Huang, B.; Dai, Y.; Frauenheim, T. High-Throughput Screening of Synergistic Transition Metal Dual-Atom Catalysts for Efficient Nitrogen Fixation. *Nano Lett.* **2021**, *21* (4), 1871–1878.

(33) Zhang, S.; Wu, J.; Zheng, M.; Jin, X.; Shen, Z.; Li, Z.; Wang, Y.; Wang, Q.; Wang, X.; Wei, H.; Zhang, J.; Wang, P.; Zhang, S.; Yu, L.; Dong, L.; Zhu, Q.; Zhang, H.; Lu, J. Fe/Cu diatomic catalysts for electrochemical nitrate reduction to ammonia. *Nat. Commun.* **2023**, *14* (1), 3634.

(34) Chen, L.; Zhang, W.; Nie, Z.; Li, S.; Pan, F. Generative models for inverse design of inorganic solid materials. *Journal of Materials Informatics* **2021**, *1* (1), 4.

(35) Yang, G.; Zhu, J.; Yuan, P.; Hu, Y.; Qu, G.; Lu, B.-A.; Xue, X.; Yin, H.; Cheng, W.; Cheng, J.; Xu, W.; Li, J.; Hu, J.; Mu, S.; Zhang, J.-N. Regulating Fe-spin state by atomically dispersed Mn-N in Fe-N-C catalysts with high oxygen reduction activity. *Nat. Commun.* **2021**, *12* (1), 1734.

(36) Li, W. H.; Yang, J.; Wang, D. Long-Range Interactions in Diatomic Catalysts Boosting Electrocatalysis. *Angew. Chem., Int. Ed.* **2022**, *61* (52), No. e202213318.

(37) Wu, J.; Li, J.-H.; Yu, Y.-X. Stabilities of group-III phosphide (MP, M = B, Al, Ga and In) monolayers in oxygen and water environments. *Phys. Chem. Chem. Phys.* **2020**, *22* (14), 7633–7642.

(38) He, T.; Santiago, A. R. P.; Kong, Y.; Ahsan, M. A.; Luque, R.; Du, A.; Pan, H. Atomically Dispersed Heteronuclear Dual-Atom Catalysts: A New Rising Star in Atomic Catalysis. *Small* **2022**, *18* (12), 2106091.

(39) Wang, Y.; Park, B. J.; Paidi, V. K.; Huang, R.; Lee, Y.; Noh, K.-J.; Lee, K.-S.; Han, J. W. Precisely Constructing Orbital Coupling-Modulated Dual-Atom Fe Pair Sites for Synergistic CO₂ Electroreduction. *ACS Energy Lett.* **2022**, *7* (2), 640–649.

(40) Liu, C.; Li, T.; Dai, X.; Zhao, J.; He, D.; Li, G.; Wang, B.; Cui, X. Catalytic Activity Enhancement on Alcohol Dehydrogenation via Directing Reaction Pathways from Single- to Double-Atom Catalysis. *J. Am. Chem. Soc.* **2022**, *144* (11), 4913–4924.

(41) Li, Y.; Shan, W.; Zachman, M. J.; Wang, M.; Hwang, S.; Tabassum, H.; Yang, J.; Yang, X.; Karakalos, S.; Feng, Z.; Wang, G.; Wu, G. Atomically Dispersed Dual-Metal Site Catalysts for Enhanced CO₂ Reduction: Mechanistic Insight into Active Site Structures. *Angew. Chem., Int. Ed.* **2022**, *61* (28), No. e202205632.

(42) Li, H.; Di, S.; Niu, P.; Wang, S.; Wang, J.; Li, L. A durable half-metallic diatomic catalyst for efficient oxygen reduction. *Energy Environ. Sci.* **2022**, *15* (4), 1601–1610.

(43) Zhu, P.; Xiong, X.; Wang, X.; Ye, C.; Li, J.; Sun, W.; Sun, X.; Jiang, J.; Zhuang, Z.; Wang, D.; Li, Y. Regulating the FeN₄ Moiety by Constructing Fe–Mo Dual-Metal Atom Sites for Efficient Electrochemical Oxygen Reduction. *Nano Lett.* **2022**, *22* (23), 9507–9515.

(44) Wu, Q.; Shen, S.; Peng, R.; Huang, B.; Dai, Y.; Ma, Y. Single-atom catalysts of TM–porphyrin for alkali oxygen batteries: reaction

mechanism and universal design principle. *J. Mater. Chem. A* **2021**, *9* (31), 16998–17005.

(45) Cheng, Y.; Dou, Y.; Zhang, X.; Song, Y.; Liu, S.; Wang, Y.; Zhang, H.; Chen, X.; Qiu, J.; Wei, Y. Oxygen Radical Anion Substituted Iron Phthalocyanine as an Effective Redox Mediator for Li–O₂ Batteries. *J. Phys. Chem. Lett.* **2023**, *14* (30), 6749–6756.

(46) Zhong, W.; Qiu, Y.; Shen, H.; Wang, X.; Yuan, J.; Jia, C.; Bi, S.; Jiang, J. Electronic Spin Moment As a Catalytic Descriptor for Fe Single-Atom Catalysts Supported on C₂N. *J. Am. Chem. Soc.* **2021**, *143* (11), 4405–4413.